

Structural Disruptions of the Outer Membranes of Gram-Negative Bacteria by Rationally Designed Amphiphilic Antimicrobial Peptides

Haoning Gong, Xuzhi Hu, Mingrui Liao, Ke Fa, Daniela Ciumac, Luke A. Clifton, Marc-Antoine Sani, Stephen M. King, Armando Maestro, Frances Separovic, Thomas A. Waigh, Hai Xu, Andrew J. McBain, and Jian Ren Lu*



Cite This: *ACS Appl. Mater. Interfaces* 2021, 13, 16062–16074



Read Online

ACCESS |



Metrics & More



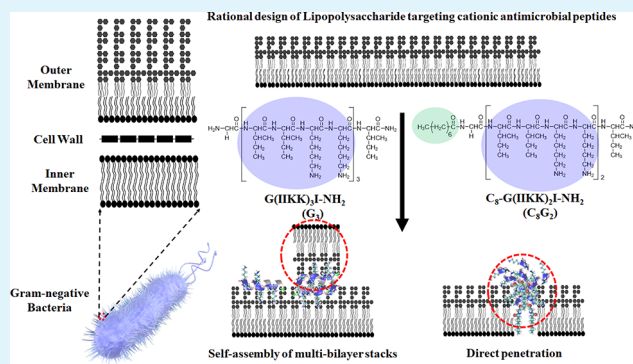
Article Recommendations



Supporting Information

ABSTRACT: Gram-negative bacteria are covered by both an inner cytoplasmic membrane (IM) and an outer membrane (OM). Antimicrobial peptides (AMPs) must first permeate through the OM and cell wall before attacking the IM to cause cytoplasmic leakage and kill the bacteria. The bacterial OM is an asymmetric bilayer with the outer leaflet primarily composed of lipopolysaccharides (LPSs) and the inner leaflet composed of phospholipids (PLs). Two cationic α -helical AMPs were designed to target Gram-negative bacteria, a full peptide $G(IKK)_3I-NH_2$ (G_3), and a hydrophobic lipopeptide $C_8-G(IKK)_2I-NH_2$ (C_8G_2 , with C_8 denoting the octanoyl chain). LPS dominates OM functions as the first line of defense against antibiotics, thereby reducing drug susceptibility. This work explores how the two AMPs interact with LPS through several carefully chosen OM models that facilitated measurements from solid-state nuclear magnetic resonance (ss-NMR), small-angle neutron scattering (SANS), and neutron reflectivity (NR). The results revealed that G_3 molecules bound preferably to the LPS head region and functioned as bridge molecules to reassemble the dislocated lipids into bilayer stacks. In contrast, C_8G_2 lipopeptides could quickly penetrate into the central region of the OM to cause direct removal of some membrane lipids. Different structural disruptions implicated different antimicrobial efficacies from these AMPs. The demonstration of the structural features underlying different susceptibilities of the OM to AMPs offers a useful route for the future development of strain-specific AMPs against antimicrobial-resistant pathogens.

KEYWORDS: antimicrobial peptides, Gram-negative bacteria, lipopolysaccharide, membrane disruption, antimicrobial resistance, infection control, small-angle neutron scattering, neutron reflectivity



1. INTRODUCTION

Antibiotics have been heralded as miracle drugs over the last century to treat infections. Unfortunately, antimicrobial resistance, exacerbated by antibiotic overuse, has compromised their effectiveness.^{1,2} Over the past few decades, novel therapeutic candidates have been explored to fight resistant bacteria, including antimicrobial peptides (AMPs).^{3,4} Many AMPs primarily work by disrupting bacterial membranes rather than targeting enzymatic, metabolic, and genetic processes by compromising the functions of intracellular targets, such as nucleic acids and proteins, as do many conventional antibiotics.^{5,6} The rapid membrane-lytic mechanism confers AMPs with broad-spectrum antimicrobial activity against both antibiotically susceptible and multi-drug-resistant bacteria, reducing the prospect of generating AMP-resistant strains.^{7–9}

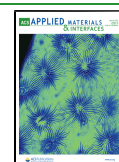
Because the bacterial cytoplasmic membrane is the main target for AMPs, previous studies have focused on exploring AMPs that disrupt the phospholipid (PL) membranes mimicking the bacterial inner membranes (IMs).^{10–14} It has

been demonstrated that AMPs co-assemble with the PL membranes via the barrel-stave pore, toroidal pore, or carpet model followed by membrane damage and leakage of intracellular contents.^{15–17} Both barrel-stave pore and toroidal pore models suggest that AMPs become inserted into the lipid bilayers. In the former, the AMPs are closely associated with the lipid hydrophobic tails, while in the latter, AMPs bend the lipids to induce further structural alterations. In contrast, AMPs in the carpet model first adsorb onto the lipid surface and subsequently remove some of them through a detergent-like mechanism after reaching a critical threshold concen-

Received: January 25, 2021

Accepted: March 23, 2021

Published: April 2, 2021



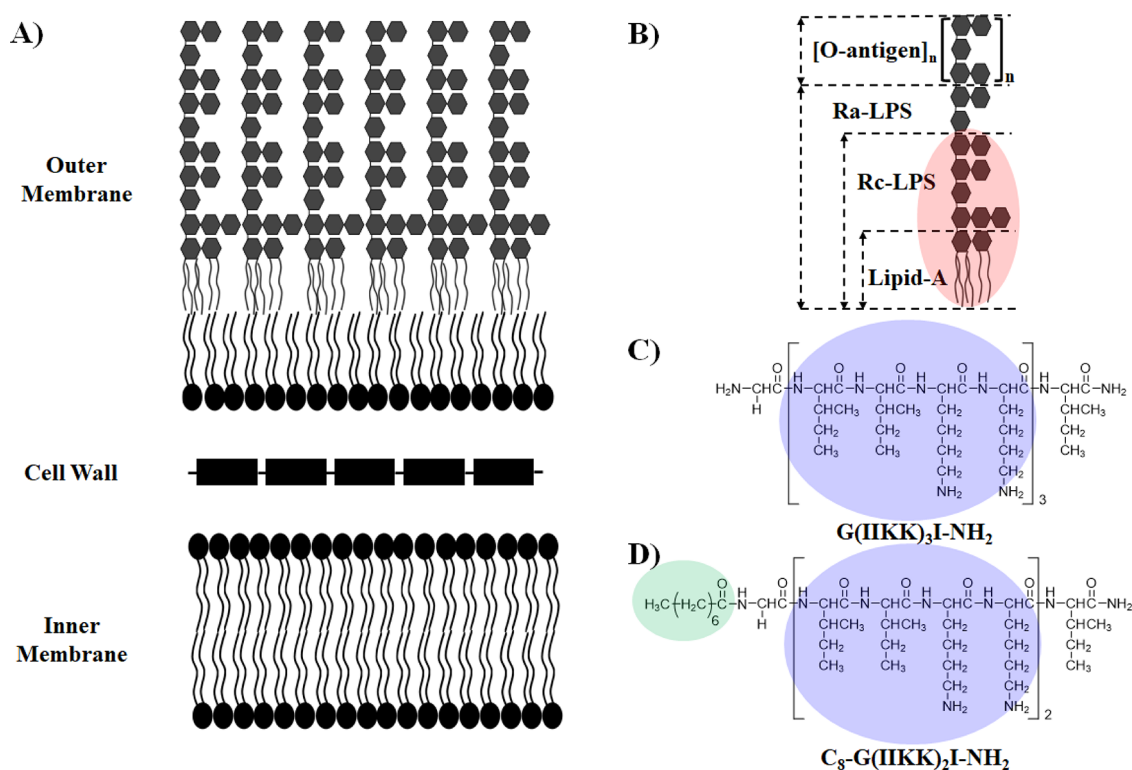


Figure 1. Schematic diagram showing the Gram-negative bacteria membrane structure and the molecular structures of AMPs. (A) The Gram-negative bacteria cell envelope is composed of a phospholipid IM, the peptidoglycan cell wall, an asymmetric OM, and additional membrane proteins (not shown). The asymmetric OM is mainly constructed of phospholipids and lipopolysaccharides (LPSs) as the inner and outer leaflets, respectively. (B) An LPS molecule contains six acyl chains in the lipid tail region and sugar groups as the lipid head region. Rough LPS constitutes the core oligosaccharide without the O-antigen part. RcLPS (red circle) was extracted from an Rc mutant *E. coli* strain and used in this research. (C,D) Molecular structures of strongly cationic G₃ and hydrophobically modified C₈G₂ amphiphilic peptides. The blue circles are IKK helical units of AMPs, and the green circle is an octanoyl chain attached to the N-terminal of the G₂ peptide.

tration. However, there is a lack of understanding of how AMPs penetrate through the bacterial outer membrane (OM) or cell wall before reaching the IMs. Advances on this front could lead to the development of novel AMPs specifically targeting either Gram-negative bacteria or Gram-positive bacteria. Recent studies have suggested that bacterial OMs play a key role in determining susceptibility to AMPs.^{18,19} For this reason, we have focused our current investigations on the interaction of AMPs with the OM, important to the development of Gram-negative bacteria specific AMPs.

The OM is asymmetric (Figure 1A) and composed of a lipopolysaccharide (LPS) outer leaflet and a phospholipid inner leaflet. An LPS molecule (Figure 1B) consists of a hydrophobic tail group (lipid A) and a hydrophilic head group (core oligosaccharide and O antigen) and is delivered to the bacterial outer surface by LPS transport proteins.^{20,21} In addition, LPS head groups are composed of repeated sugar units (e.g., heptose, KDO, etc.)²² and anionic phosphate groups and are bridged by divalent cations (e.g., Ca²⁺ or Mg²⁺).²³ Due to its amphiphilic nature, the LPS outer membrane functions as a selective barrier to maintain the cell structure and ensure the bacterium's ability to survive even in the harshest environments.^{24,25} Therefore, destroying the LPS membrane is important to fight Gram-negative bacteria and could be achieved by antibiotics that target the biosynthesis of LPS, or the transport genes of LPS, or the physical disruption of the anionic LPS membrane itself by AMP binding.

Either the hydrophilic polysaccharide core or hydrophobic acyl chains of LPS could be potential barriers that prevent drug binding and transport across the cell wall. For example, LPS is found to inhibit binding and pore-formation by an antibacterial protein RegIIIα since the protein has an insufficient number of positive charges.²⁶ The polyanionic LPS membranes also prevent the entry of many small hydrophobic molecules from entering the acyl chain region of the OM.^{24,25} Therefore, an AMP must carry sufficient positive charges to bind to the LPS surface by electrostatic interactions and possess appropriate hydrophobicity to insert into the membrane.

Among many AMPs that specifically kill Gram-negative bacteria, a naturally occurring lipopeptide, polymyxin B, is speculated to disrupt LPS membranes.^{18,27} A polymyxin B molecule has a polycationic cyclic peptide head that facilitates binding to the LPS head groups and an hydrophobic acyl chain that can help insertion into the LPS lipid A region.²⁷ However, it remains unclear how positive charges and hydrophobicity of an AMP influence the action against the bacterial OM.

To investigate the design strategy of AMPs that is critical for killing Gram-negative bacteria, interactions of two rationally designed AMPs against bacterial LPS OM models have been systematically studied. G(IKK)₃I-NH₂ (G₃, Figure 1C) was developed as an α-helical cationic AMP, which has shown broad-spectrum antibacterial and antitumor activities, while demonstrating good biocompatibility with host human red blood cells (hRBCs).^{28–30} It has six lysine residues out of the 14 amino acids, providing +7 positive charges at physiological pH and high affinity for negatively charged bacterial

membranes. Furthermore, an acyl chain incorporated lipopeptide C₈-G(IKK)₂I-NH₂ (C₈G₂, Figure 1D) was designed to provide stronger hydrophobicity but has a shorter peptide sequence.^{31,32} A range of *in vitro* models including LPS/PL vesicles, LPS monolayers, and LPS/PL asymmetric bilayers have been chosen to facilitate a range of experimental techniques to probe their interactions with G₃ and C₈G₂. Circular dichroism (CD) and Fourier transform infrared spectroscopy (FTIR) illustrated that both G₃ and C₈G₂ had a high proportion of α -helical content after interacting with LPS model membranes. The locations of the AMPs in the LPS membranes and their subsequent structural impacts were demonstrated by small-angle neutron scattering (SANS) and neutron reflectivity (NR). The more cationic G₃ had a strong tendency to associate with LPS head regions, disrupting LPS membranes and subsequently reassembling some lipids into adherent bilayer stacks. In contrast, the more hydrophobic C₈G₂ was less selective against PL or LPS and became directly inserted into the lipid tail region, causing different structural disruptions. Manipulating AMP cationicity and hydrophobicity critically determines their membrane-targeting (IM or OM) and leads to an imbalanced osmotic pressure and cell rupture due to membrane damage. These results could provide useful guideline for the development of AMPs specifically against Gram-negative bacteria.

2. EXPERIMENTAL SECTION

2.1. Materials. Phospholipids including 1,2-dipalmitoyl-*sn*-glycero-3-phosphocholine (DPPC), 1-palmitoyl-2-oleoyl-*sn*-glycero-3-phospho-(1'-*rac*-glycerol) (POPG), and 1-palmitoyl-2-oleoyl-*sn*-glycero-3-phosphocholine (POPC) were purchased from Avanti Polar Lipids unless otherwise stated. Hydrogenated phospholipids were denoted as hDPPC, hPOPG, and hPOPC. Acyl chain deuterated phospholipids were labeled as d₆₂-DPPC, d₃₁-POPG, and d₃₁-POPC (simplified as dDPPC, dPOPG, dPOPC). All peptides were purchased from Shanghai TopPeptide Company (>98% purity). G₃ and C₈G₂ were analyzed by reversed-phase high-performance liquid chromatography (RP-HPLC) and matrix-assisted laser desorption/ionization mass spectrometry (MALDI-MS) for purity and molecular weight determinations, as demonstrated in Section S1 of the Supporting Information. All other chemical reagents were purchased from Sigma-Aldrich and were used as provided unless otherwise stated.

2.2. LPS Deuteration and Extraction. Hydrogenated and deuterated Rough C LPS (hRcLPS/dRcLPS or hLPS/dLPS) were extracted from an *Escherichia coli* J5 strain (ATCC 43745) following the procedures described by Le Brun *et al.*³³ The use of a rough type LPS facilitated the formation of lipid bilayers and studies of AMP binding.^{34,35} The ModC1 media, as prepared in either H₂O or D₂O, were used for bacterial culture and fermentation.³³ Phenol red (4 μ g/mL) was added in the ModC1 media to indicate the solution pH. *E. coli* J5 cells from the glycerol stock were first revived in H₂O, and then H₂O was stepwise replaced with D₂O to produce D₂O-resistant bacteria, i.e., increasing the proportion of D₂O daily to 25, 50, 75, and 100%. Thereafter, D₂O-adapted *E. coli* was inoculated into a 2 L Duran bottle with 1 L of D₂O ModC1 media and incubated at 37 °C. A pump was used to deliver air into the Duran bottles, with a 0.2 μ m pore-size filter to filter the air. Wet *E. coli* cells were collected daily by centrifugation (1000g, 5 min), with the addition of ammonium hydroxide and supplementary glycerol to control the solution pH at 7 and provide the carbon source, respectively. About 20 g of hydrogenated and deuterated *E. coli* wet cells were collected in total. Hydrogenated and deuterated cells were washed with H₂O or D₂O, respectively, and collected by centrifugation followed by ethanol washing and centrifugation. The washing procedures were conducted three times to minimize salt impurities. Dried cells were collected by freeze drying overnight before LPS extractions.

Hydrogenated and deuterated RcLPS were extracted using a phenol/chloroform/petroleum ether (2/5/8, v/v/v) method.^{33,36} Each 1 g of the dry cells was homogenized in 10 mL of the phenol/chloroform/petroleum ether mixtures. A stirrer was used to properly mix the suspension to facilitate cell destruction and LPS solubility. The homogenate was centrifuged at 3600g for 20 min, and the supernatant (light yellow) was collected by filtration through a coarse filter paper to avoid bacterial pellets. Extractions of RcLPS from bacterial pellets were repeated three times. Thereafter, chloroform and petroleum ether were removed by a rotary evaporator. The diethyl ether/acetone (1/1, v/v) was titrated to the phenolic solution until the appearance of insoluble RcLPS precipitates. The solutions were centrifuged at 3600g for 30 min, and the RcLPS precipitates were collected by discarding the supernatant. A small amount of phenol/water mixture (4/1, w/w) was used to wash the RcLPS pellets followed by titrations of diethyl ether and centrifugation (3600g, 30 min.). Triplicate washing procedures were undertaken to properly remove protein and nucleic acid components. The solvent residues were freeze-dried, and light yellow RcLPS was collected.

The crude products were homogenized in H₂O (hRcLPS) and D₂O (dRcLPS) at 20 mg/mL and sonicated at 45 °C for 1 h. The pure RcLPS was precipitated by ultracentrifugation at 100,000g for 4 h using a Beckman MLA-80 ultracentrifuge. The RcLPS pellets were collected by discarding the yellowish supernatants and freeze-drying overnight. The quality of the extracted hRcLPS and dRcLPS was compared with that of the RcLPS product (denoted as sRcLPS) from Sigma-Aldrich and examined using MALDI-MS, Bradford assay, and KDO assay as shown in Figures S1 and S2.

2.3. Antimicrobial Assays. *Escherichia coli* (*E. coli*, ATCC 43745 & 25922) was used for antimicrobial susceptibility tests, including measurements of minimum inhibitory concentration (MIC) and dynamic kills.^{37,38} A single bacterial colony was inoculated into Mueller Hinton broth (MHB) and cultured overnight at 37 °C. The overnight bacterial culture was diluted to 1 \times 10⁶ CFU/mL using MHB before interaction with AMPs. AMPs were prepared in standard phosphate-buffered saline (PBS) solution (10 mM phosphate buffer, 2.7 mM KCl, 137 NaCl, pH 7.4). AMP solutions were double-diluted into 96-well plates and properly mixed with diluted bacterial culture (100 μ L AMP + 100 μ L bacteria). The positive and negative controls used were fresh bacterial culture (100% growth) and MHB broth (0% growth), respectively. The 96-well plates were incubated overnight (18–24 h) at 37 °C. The solution turbidity, as measured by the optical density reading at 600 nm (OD₆₀₀), was used to estimate the bacterial survival fraction: survival fraction = (OD_{600, peptide} - OD_{600, negative}) / (OD_{600, positive} - OD_{600, negative}) \times 100. OD₆₀₀ was measured by a Sunrise absorbance microplate reader (Tecan, Switzerland). The lowest AMP concentration to observe no bacterial growth was defined as the MIC. Each MIC measurement had nine replicates (three independent repeats and three technical repeats in each experiment).

Dynamic kills were performed by mixing the bacterial culture and AMPs in PBS buffer and then streaked onto the Mueller Hinton agar (MHA) after interactions for set time points. The initial bacterial density was 1 \times 10⁶ CFU/mL, and the AMP concentrations were \times 2, \times 4, and \times 10 MICs. After incubations of MHA overnight at 37 °C, the bacterial colonies that had survived were counted. Each dynamic kill curve was repeated three times.

2.4. Hemolytic Activity. Human red blood cells (hRBCs) were purchased from the Rockland Immunochemical Inc. (Limerick, USA) for cell toxicity tests. Two-fold PBS-diluted AMP solutions (100 μ L) were pipetted into 96-well plates followed by the addition of 4% hRBCs in PBS (100 μ L). Fresh hRBCs with 0% leakage and hRBCs 100% ruptured by 0.1% Triton X-100 were negative and positive controls, respectively. The 96-well plates were incubated for 1 h at 37 °C. The 96-well plates were centrifuged at 1000g for 5 min to collect supernatants for measurements of hemoglobin release. The percentage of hemoglobin leakage was determined by leakage = (A_{450, peptide} - A_{450, negative}) / (A_{450, positive} - A_{450, negative}) \times 100. A₄₅₀ denotes the optical absorbance at 450 nm as measured using a

Tecan Sunrise absorbance microplate reader. The hRBC survival fraction was calculated using survival fraction = 100 – leakage. Each hemolysis assay had nine replicates (three independent repeats and three technical repeats in each measurement).

2.5. Preparation of Small Unilamellar Vesicles (SUVs). POPG/POPC (3:7, mol/mol) and RCLPS/POPC (1:9, mol/mol) were used to mimic the bacterial inner and outer membrane composition, respectively.^{39,40} The molar ratio of 1:9, RCLPS/POPC, had an equivalent mass ratio of about 3:7, which was similar to the POPG/POPC system. Lipids were properly mixed in the solvent (chloroform/methanol, 9:1, v/v) and freeze-dried. The lipid mixtures were suspended in HEPES buffer (20 mM, pH 7.4) and sonicated for 10 min. The SUVs were produced by extruding lipids through a 50 nm polycarbonate filtration membrane 31 times as previously described.^{40,41} SUVs were then interacted with AMPs and analyzed by dynamic light scattering (DLS), circular dichroism (CD), and SANS.

2.6. CD. AMPs were dissolved in HEPES buffer (20 mM, pH 7.4) and interacted with POPG/POPC (3:7, mol/mol) SUVs and RCLPS/POPC (1:9, mol/mol) SUVs. The final AMP concentration was 0.1 mM, and the SUV concentration was 1 mM. CD spectra were acquired using a Chirascan Series Spectrometer (Applied Photo-physics, UK) at 37 °C. The sample path length was 0.2 mm, the scan speed was 60 nm/min, and the wavelength range was 190–260 nm.

2.7. SANS. SANS experiments were performed using the LOQ diffractometer at the ISIS Pulsed Neutron Source (STFC Rutherford Appleton Laboratory, Didcot, UK) using the same experimental configuration as previously described.^{42,43} SUVs were prepared in D₂O HEPES buffer (20 mM, pH 7.4) and then mixed with AMP solutions for SANS measurements. Samples were measured at 37 °C. The final SUV concentration was 1 mM, and AMP concentrations were 0.05, 0.1, and 0.2 mM. Each SANS measurement was performed once. Correction and azimuthal averaging of the as-measured SANS data were performed in the Mantid framework (www.mantidproject.org). Reduced SANS data were then fit with a core multilayer shell model (http://www.sasview.org/sasview/user/models/model_functions.html#coremultishellmodel) using the SasView 5.0 software (www.sasview.org). The length scale characterized by the Bragg peak was calculated using $L = \frac{2\pi}{Q}$, where Q in SANS and NR is the magnitude of the neutron momentum transfer. All the fit parameters are shown in Tables S1–S4 of the Supporting Information.

2.8. Solid-State Nuclear Magnetic Resonance (ss-NMR). Hydrogenated RCLPS was mixed with single chain deuterated POPC (d₃₁-POPC, denoted as d-POPC) at a molar ratio of 1:9 to mimic the bacterial OM. 10 mg of the lipid sample was suspended in 1 mL of water, and the AMP was added (AMP/lipid = 1:5, mol/mol). Samples were freeze-dried and resuspended into HEPES buffer (20 mM, pH 7.4) to reach 70% hydration (sample/water = 3:7, w/w). Three freeze–thaw cycles were performed before transferring into a 4 mm zirconia NMR rotor for ss-NMR experiments.

A 400 MHz Bruker Advance III NMR spectrometer (Wissembourg, France) was used for ss-NMR experiments following the same procedures as previously described.^{32,44} Static ³¹P and ²H ss-NMR runs were performed at 37 °C with frequencies of 161.5 and 61.5 MHz, respectively. Data analysis was performed using the Bruker TopSpin software 4.0.7 (www.bruker.com).

2.9. LPS Monolayer. RCLPS monolayers were constructed at the air/liquid interface using a Langmuir trough (12.5 × 15 cm, Nima Technology, Biolin Scientific, Finland) as previously stated.^{10–12} The Langmuir trough contained 70 mL of HEPES buffer (20 mM, pH 7.4). Lyophilized RCLPS was suspended in the chloroform/methanol/water mixture (60:35:5, v/v/v) at 1 mg/mL and carefully spread onto the water surface followed by solvent evaporation for 15 min. The initial surface pressure was controlled at 28 mN/m under equilibrium conditions. Thereafter, peptide solutions were injected underneath the lipid monolayers to give a final concentration of 30 μM. The lipid monolayers before and after interaction with AMPs were measured by NR and external reflection Fourier transform infrared spectroscopy (ER-FTIR). In NR experiments, each data set consisted of four

isotopic contrasts, i.e., hRCLPS/dRCLPS on NRW/D₂O. Each contrast was measured once. The lipid monolayer experiments were performed at 20 °C to avoid water evaporation during the experiments.

2.10. Asymmetric LPS/DPPC Bilayer. The asymmetric RCLPS/DPPC bilayers were deposited on the surface of polished optically flat silicon blocks using a custom-built Langmuir–Blodgett (LB) trough (Nima Technology) as previously described.¹⁸ DPPC was dissolved in a chloroform/methanol mixture (9:1, v/v) at 1 mg/mL and spread on the surface of buffered water (HEPES 20 mM, CaCl₂ 5 mM, pH 7.4, 10 °C) with the surface pressure controlled at 35 mN/m. The choice of the gel-phased DPPC monolayer, deposition at low temperature, and addition of calcium were helpful for inner leaflet stabilization and facilitated further coating by the LPS outer leaflet.²³ A previously submerged silicon block was lifted vertically at a speed of 4 mm/min, while the surface pressure was kept at 35 mN/m. Therefore, an inner DPPC leaflet was deposited on the silicon surface via the process of Langmuir–Blodgett deposition. Afterward, the Langmuir trough was cleaned followed by pouring buffer to construct the air/liquid interface under the same conditions (10 °C). RCLPS (1 mg/mL) suspended in the chloroform/methanol/water mixture (60:35:5, v/v/v) was spread on the buffer surface and compressed to 35 mN/m until stabilized. An outer RCLPS leaflet was deposited outside the DPPC monolayer by dipping the silicon block horizontally using the Langmuir–Schaeffer (LS) deposition process. The dipper speed was 4 mm/min, and the silicon block was assembled with the sample cell under water. Each RCLPS/DPPC bilayer was first scanned by NR at 20 °C and then at 37 °C to check the bilayer quality. Thereafter, AMP solutions at 10 μM were injected into the sample cell to interact with the bilayer using a liquid chromatography pump (Hitachi L7100 HPLC pump) followed by NR scanning at 37 °C. To better characterize the locations of lipids and AMPs, six isotopic contrasts were measured. Each AMP (dissolved in D₂O, water contrast matched to silicon (CMSi, D₂O/H₂O = 38:62, v/v), H₂O) interacted with two bilayers (hRCLPS/dDPPC and dRCLPS/dDPPC), respectively, to complete the contrast variations.

2.11. NR. Specular neutron reflectivity (NR) experiments (air/liquid and solid/liquid interfaces) were performed using the SURF and INTER reflectometers at the ISIS Pulsed Neutron Source (STFC Rutherford Appleton Laboratory, Didcot, UK)⁴⁵ and the FIGARO reflectometer at the Institute Laue Langevin (Grenoble, France).⁴⁶ Samples were scanned on SURF at three incident angles (0.35, 0.65, 1.5°), on INTER at two incident angles (0.7, 2.3°), and on FIGARO at two incident angles (0.62, 3.8°). These instruments all covered an effective momentum transfer range (Q -range) of 0.01–0.3 Å^{−1} used in NR data analysis.

NR data was analyzed using the Motofit package.⁴⁷ The lipid monolayers or bilayers at the interfaces were modeled as a series of homogeneous slabs layered along the surface normal direction (denoted herein as the z -axis). Each layer was characterized by a thickness (τ), a scattering length density (SLD, denoted as ρ), and a roughness. The roughness was fixed as 1 Å in the NR analysis. Each set of NR data had multiple isotopic contrasts (four in monolayers and six in bilayers), as described above, to highlight different SLD values in different layers. In each layer, the SLDs can be used to calculate the sample volume fraction (ϕ): $\rho_{\text{fit}} = \sum_n \rho_n \phi_n$, where n is an index indicating the molecular composition in the layer, which includes solvent, peptide, lipid head, lipid tail, etc. The total volume fraction in each layer must be 1, i.e., $\sum_n \phi_n = 1$. Each reflectivity data set was fitted to a single set of the structural parameters (mean values including layer thickness and sample volume fraction), with errors indicating the standard deviations of different contrasts. The typical errors in NR were within 5–10% of the mean values. The sample surface concentration can be derived as $\Gamma = \frac{\rho \tau \phi}{b N_A}$, where b is the neutron scattering length of the sample and N_A is Avogadro's number. The area per molecule (A) of a component was calculated using $A = \frac{b}{\rho \tau \phi}$.

3. RESULTS

3.1. Peptide Design, Antimicrobial Activity, and Cell Cytotoxicity. The amino acids used in constructing G_3 and C_8G_2 were hydrophobic isoleucine (I) and cationic lysine (K), based on IIKK repeat units that tend to adopt α -helical conformations upon binding with bacterial membranes.²⁸ The G_3 peptide has 3 IIKK repeats, containing 6 Ks and 7 Is and carrying +7 charges at physiological pH. By contrast, C_8G_2 only has 2 IIKK repeats, containing 4 Ks and 5 Is and carrying +4 charges. C_8G_2 is a weaker version of G_3 in terms of fewer IIKK helical repeats, but the attachment of the hydrophobic C_8 acyl chain to its N-terminus boosts its hydrophobicity. Thus, a C_8G_2 molecule is more hydrophobic than G_3 but carries less positive charge, which tends to encourage self-assembly into nanostructure-based hydrogels.³¹ RP-HPLC measurements revealed that G_3 and C_8G_2 had retention times of 19.3 and 23.5 min, respectively, consistent with the notion that a higher retention time indicates stronger hydrophobicity.

We first tested the antibacterial activity and hemolytic activity of the designed AMPs. As shown in Figure 2A, the

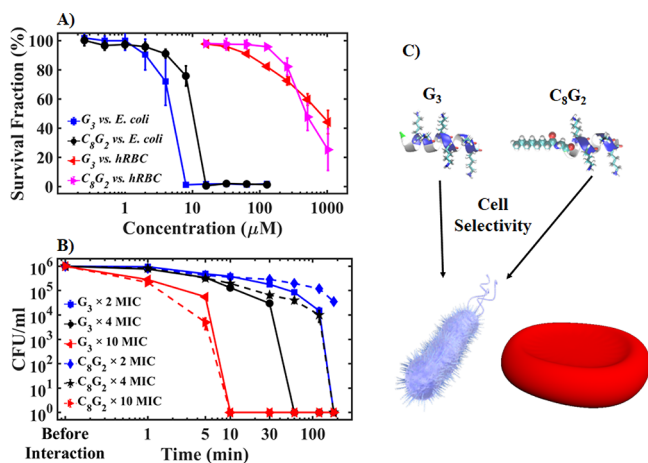


Figure 2. *In vitro* antibacterial and cell toxicity assays. (A) Survival fractions of *E. coli* (ATCC 43745) and hRBCs when incubated with G_3 and C_8G_2 AMPs using antibacterial and hemolytic assays. (B) Dynamic killing of *E. coli* by G_3 and C_8G_2 at different initial concentrations. (C) A schematic diagram to demonstrate that G_3 and C_8G_2 AMPs selectively kill bacteria with low toxicity to the hRBCs. Green, white, blue, and cyan in the helical peptide molecules represent glycine, isoleucine, lysine, and hydrocarbon chains, respectively. The MIC measurements and the hemolytic assays were repeated three times, and each experiment consisted of three technical repeats. Each bacterial dynamic killing experiment had three replicates. Mean \pm standard deviations were calculated based on the replicates.

MICs of G_3 and C_8G_2 against *E. coli* (ATCC 43745) were 8 ± 2 and 16 ± 4 μ M, respectively, suggesting potent antibacterial activities for both. It was found that at or just above these AMP concentrations, no sign of bacterial regrowth could be found during measurement over the subsequent 48 h.

Hemolysis analysis revealed that up to 5–10 \times MICs, neither AMP shows obvious cytotoxicity against hRBCs. With a further increase of AMP concentration, G_3 displayed a gradual concentration-dependent development of hemolytic activity. In contrast, C_8G_2 presented a different concentration-dependent response. The almost zero impact on toxicity occurred up to about 100 μ M, above the point at which the fraction of

concentration-dependent cytotoxicity intensified as indicated from the release of hemoglobin from hRBCs. At 250 μ M, the two AMPs had the same cytotoxicity, and then C_8G_2 exceeded G_3 as the concentration further increased. The inner membrane of hRBCs carries weak negative charges,⁸ which may have greater attraction for the strongly cationic G_3 at low peptide concentrations. As the AMP concentration is further increased, C_8G_2 lipopeptides may bind preferably to the surface of hRBCs and disrupt membranes through strong hydrophobic interaction. The greater cytotoxicity of C_8G_2 at high concentrations may be due to its more hydrophobic nature and nonspecific attack on the integrity of membranes. G_3 and C_8G_2 cause 50% hemoglobin release (EC_{50}) at 650 ± 90 and 550 ± 50 μ M, respectively. Given that their MICs are 8 ± 2 and 16 ± 4 μ M, respectively, G_3 and C_8G_2 have selectivity indices (SIs) of 81 and 34 ($=EC_{50}/MIC$).

For many practical applications, such as wound treatments, antimicrobial drugs are expected to rapidly eradicate infective pathogens. As shown in Figure 2B, G_3 and C_8G_2 displayed concentration-dependent dynamic killing when incubated for different periods. At a low concentration of 2 \times MIC, at least 3 h was needed for G_3 and C_8G_2 to completely kill the *E. coli*. At 10 \times MIC, *E. coli* colonies were significantly reduced after 1 min of exposure, and complete eradication was achieved within 10 min. For the same dynamic assays using traditional antibiotics, such as ampicillin, less than 90% *E. coli* was killed after 3 h of exposure at 10 \times MIC.¹² Therefore, the designed AMPs (especially G_3) have the advantage of rapid deactivation of *E. coli* under short exposures, indicating a lower likelihood to produce AMP-resistant strains.³⁰ This feature of high antimicrobial efficacy under short contact times is useful for many types of infection controls, especially topical hygiene and wound treatment.

3.2. Interaction with SUVs. Although the antibacterial mechanism of cationic AMPs is widely ascribed as due to membrane disruption, the detailed understanding of the molecular mechanism of AMP action against different bacteria is still lacking. These structural features are crucial for the development of potent strain-specific AMPs. As described previously, G_3 and C_8G_2 were purposely designed to possess both strong cationic and hydrophobic characters. It is expected that polyanionic LPS molecules, forming the outer leaflet of the outer membrane, are the main targets of these AMPs.⁴⁸ In this study, LPS directly extracted from *E. coli* (Rc mutant strain) was used to constitute different bacterial OM models, with the composition of LPS/POPC (1:9, mol/mol) used as a mimic of the bacterial OM. In contrast, a 30% negatively charged lipid model, consisting of POPG/POPC (3:7, mol/mol), was used to mimic the bacterial IM.⁸ The different molar ratios adopted for the negatively charged lipids of POPG and LPS actually resulted in almost the same mass ratio in the IM and OM models. Thus, their susceptibilities under exposure to the two AMPs can be better understood by the interaction intensities under the same AMP concentrations. The use of unsaturated and uncharged POPC component in SUVs facilitated the preparation and stabilization of SUVs under the study.

In Figure 3A,B, under buffered conditions or mixed with uncharged POPC SUVs (not shown), G_3 and C_8G_2 existed as random-coiled monomers, indicated by the single CD minimum at 200 nm. The similarity in CD spectra under these conditions suggests no response of the AMP to the uncharged membranes, with little or no membrane-lytic

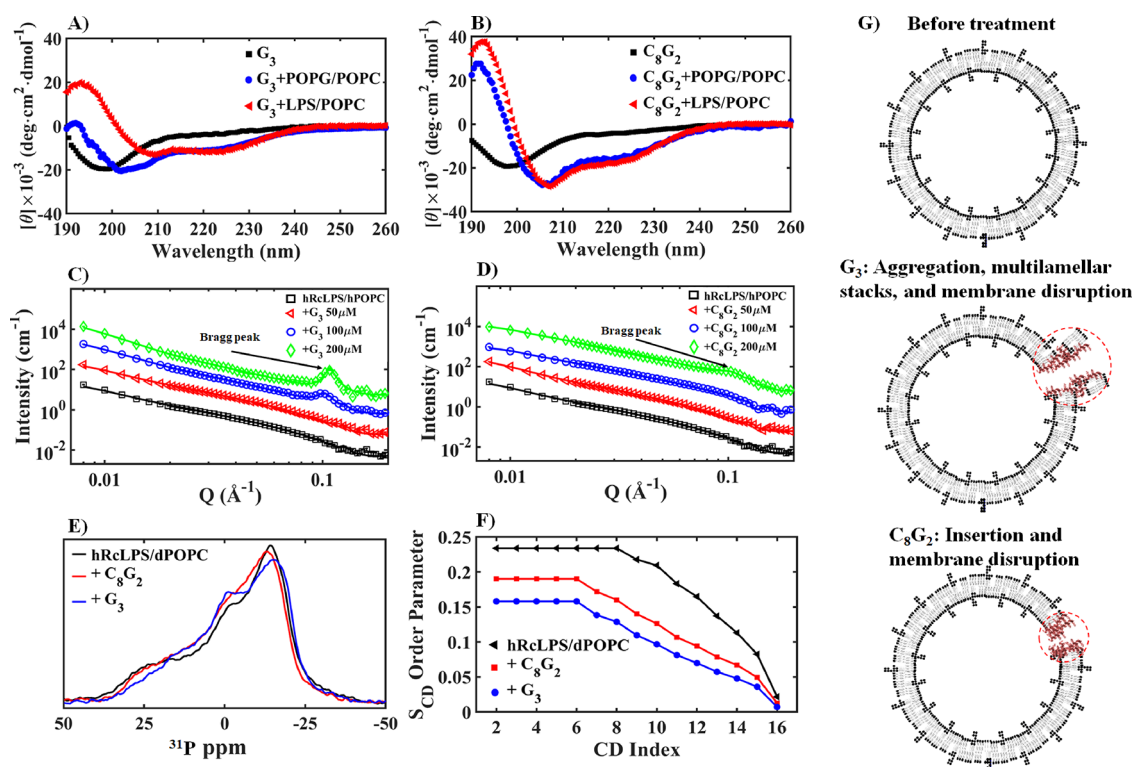


Figure 3. Vesicular models and their characterizations. CD spectra of (A) G_3 and (B) C_8G_2 in buffer and after interaction with POPG/POPC (3:7, mol/mol) and LPS/POPC (1:9, mol/mol) vesicles. G_3 and C_8G_2 in the uncharged POPC vesicles and in buffer conditions had similar CD spectra. Peptide concentrations were 0.1 mM, and vesicle concentrations were 0.5 mM, i.e., a peptide/lipid molar ratio of 1:5. (C,D) SANS intensity data from hLPS/hPOPC (1:9, mol/mol) vesicles at 1 mM with and without G_3 and C_8G_2 at various concentrations. (E) ss-NMR ^{31}P spectra of hLPS/dPOPC MLVs (black) interacting with C_8G_2 (red) and G_3 (blue). G_3 disrupted POPC/LPS bilayers with the formation of a small isotropic peak. (F) S_{CD} order parameters derived from the quadrupolar splittings of ^2H NMR spectra (Figure S4). The deuterated POPC acyl chains were more disordered after interaction with G_3 and C_8G_2 . (G) Schematic diagrams to illustrate the mechanistic processes of structural changes to the bilayer of the OM vesicle caused by AMP binding.

activity. However, upon exposure to POPG/POPC SUVs, G_3 and C_8G_2 transformed into α -helical conformations, characterized by the CD double minima at 208 and 222 nm.⁴⁹ The transition to the α -helical structure likely results in AMP molecules adopting an amphiphilic structure and aggregating on the lipid surface with a stronger capability to cause damage to bacterial membranes.¹² These secondary structural changes are consistent with strong interactions between AMPs and anionic bacterial membranes.

SUVs before and after interaction with AMPs were analyzed by SANS for morphological structural changes, and the results are shown in Tables S3 and S4. Both POPG/POPC and LPS/POPC SUVs could be treated as spheres with a single lipid bilayer encapsulation. This vesicular model is characterized by the radius of the sphere and a symmetrical lipid bilayer consisting of the outer head region, the middle acyl chain region, and the inner head region. The SANS profiles from the vesicles exposed to G_3 and C_8G_2 at the highest tested concentration of 200 μM (peptide/lipid molar ratio = 1:5) were compared with that from the POPG/POPC SUVs alone (Figure S3). The difference was small, showing little impact on the bacterial IM model from AMP binding. The POPG/POPC vesicles could be best represented as having a radius of 370 ± 15 Å from data fits to the SANS profiles. The radii and the bilayer thicknesses changed little with increasing AMP binding. The head layers were 7 ± 1 Å, and the middle acyl layers were 27 ± 2 Å, leading to a total bilayer thickness of 41 ± 4 Å.

Notably, the SLD values for the acyl chain layers did increase, indicating AMP binding.

When the same fit model was applied to the LPS/POPC SUVs, the head layer was 15 ± 1 Å and the acyl tail layer was 26 ± 2 Å, close to that of the POPG/POPC bilayer. The total bilayer thickness was 56 ± 4 Å, and the thicker head region is clearly due to the bulkier LPS head groups. Upon binding of G_3 , the overall SUV structure changed little, but as the G_3 concentration increased to 100 and 200 μM , restructuring occurred in the LPS/POPC vesicles due to AMP attack, transforming some of the single bilayer into multi-bilayer membrane stacks, as reflected by the Bragg peaks in the SANS profiles (Figure 3C,D). The Bragg peaks have a characteristic Q -position of 0.105 ± 0.003 Å⁻¹, indicating a 60 Å ($=2\pi/Q$) size for the repeating unit (bilayer and water gap).⁵⁰ The intensity of the Bragg peak (or full width at half-maximum FWHM) is relevant to the number of elements in the stack (for perfect crystalline ordering, it scales as N^2 , where N is the number of elements). The SANS data revealed that more additional bilayer stacks were formed when treated with G_3 , especially at the highest tested concentration with an intense Bragg peak. Therefore, G_3 was more likely to cause fusion of the model bacterial OM.

In comparison, the Bragg peaks in the SANS profiles upon C_8G_2 binding are less pronounced, though visible at the two high concentrations. As will be discussed later, this is because C_8G_2 is more likely to insert into the middle acyl region of vesicles and cause a different type of removal of membrane

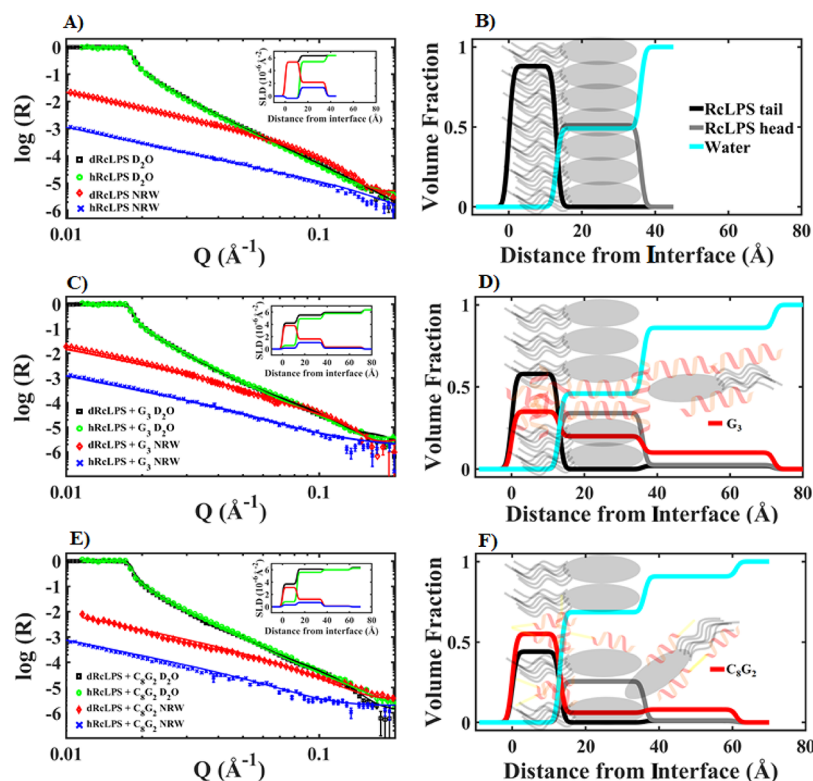


Figure 4. NR data and analyses from AMP binding to spread LPS monolayers. NR profiles of (A,B) LPS monolayers at the air/liquid interface and after interaction with (C,D) G_3 and (E,F) C_8G_2 as a function of neutron momentum transfer, Q , perpendicular to the interface. The continuous lines in panels (A), (C), and (E) represent the best reflectivity model fits, and the inset figures are the derived SLD distributions along the z -axis. The volume fraction distributions in panels (B), (D), and (F) were calculated as described using the theoretical SLDs of different components as listed in Tables S1 and S2. The initial surface pressure of the LPS monolayer was 28 mN/m, and the AMP concentration was 30 μ M.

lipids via C_8G_2 -assisted dispersion. It can be seen from Table S4 that different layers of vesicles became progressively overlapped, with the overall bilayer remaining constant at 55–57 Å. The thickness of acyl tail layer was reduced from 25 ± 2 to 21 ± 2 Å, and the thickness of the head layer increased from 15 ± 1 to 17 ± 1 Å.

3.3. Solid-State Nuclear Magnetic Resonance. The local order of phosphate groups and deuterium-carbon chains in hLPS/dPOPC multilamellar vesicles (MLVs) were determined using ^{31}P and ^2H ss-NMR spectra. The static ^{31}P NMR spectra in Figure 3E indicate the orientation and dynamics of the phosphate head groups in LPS/POPC vesicles. Vesicles composed of LPS/POPC had similar chemical shift anisotropy (CSA) values before and after interaction with G_3 and C_8G_2 , with an overall powder pattern spectral width of ~ 45 ppm, typical for a fluid bilayer. This suggests that neither G_3 nor C_8G_2 strongly affects the dynamics and orientation of the lipid head groups. However, vesicles after incubation with G_3 showed a small isotropic peak at ~ 0 ppm (Figure 3E), indicating the formation of small isotropically tumbling lipid aggregates promoted by interaction with G_3 .⁵¹

The static ^2H NMR spectra in Figure S4 demonstrated a significant perturbation of the lipid acyl chains (C16 deuterated POPC) by G_3 and C_8G_2 AMPs. Carbon-deuterium order (S_{CD}) parameters in Figure 3F of each individual deuterated position in POPC were calculated based on the line splittings shown in Figure S4. Both G_3 and C_8G_2 had significant effects on the acyl chains of LPS/POPC MLVs as observed by the reduced S_{CD} values. The reduction in S_{CD}

values indicates that AMPs increased the motion throughout the lipid acyl chain. The S_{CD} proximal to the glycerol backbone was reduced from 0.233 to 0.190 and 0.158 after interaction with C_8G_2 and G_3 , respectively, equivalent to a 19 and 32% reduction in order. Both peptides disturbed the hydrophobic core of the bilayer down to the terminal C16 carbon, which showed an even more drastic reduction of the order parameter from 0.022 (MLVs only) to 0.013 (+ C_8G_2) and 0.007 (+ G_3), i.e., 41 and 68% of the reduction in the middle of the bilayer, respectively. Therefore, both designed AMPs had the capability to insert deeply into the lipid bilayers, and the more cationic G_3 showed a greater impact than the hydrophobic C_8G_2 either in the lipid head or tail groups.

3.4. Lipid Monolayer Model. To better characterize the extracted deuterated and hydrogenated RCLPS (denoted as dLPS and hLPS) from *E. coli* and understand LPS-AMP interactions, planar lipid monolayers were spread using a Langmuir trough and allowed to interact with G_3 and C_8G_2 . LPS monolayers at the air/liquid interface were first studied using surface pressure, FTIR, and NR. The LPS monolayers were controlled at an initial surface pressure of 28 mN/m to achieve a lateral compression similar to that observed with natural membranes while retaining membrane stability and avoiding collapse.³³ In the NR experiments, dLPS or hLPS was spread on null reflecting water (NRW; i.e., $\rho = 0$) or D_2O to allow parallel NR measurements using four isotopic contrasts (Figure 4A), which highlighted either the lipids or the water in the monolayer system via deuteration. Simultaneous fits of the reflectivity data under the four contrasts help to determine the location and amount of either lipids or peptides as a function

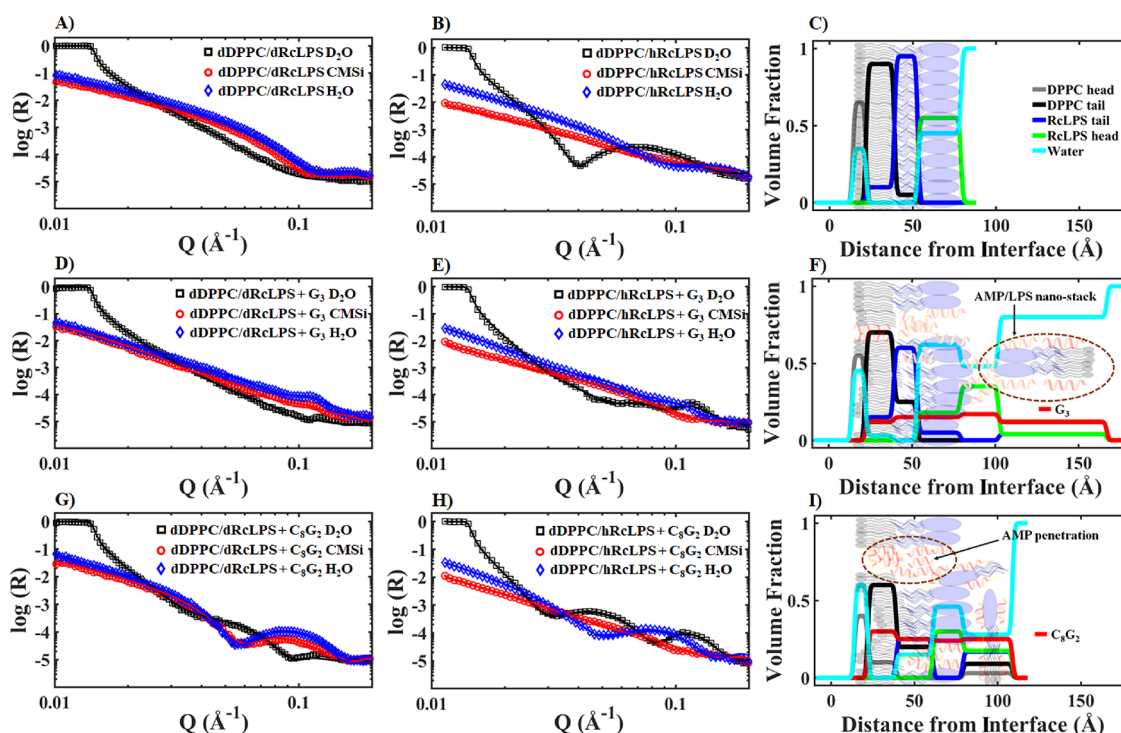


Figure 5. NR data and analyses from supported asymmetric bilayers. (A–C) RcLPS/DPPC bilayers at the solid/liquid interface, (D–F) upon interaction with G_3 , and (G–I) with C_8G_2 . Panels (A), (B), (D), (E), (G), and (H) show the logarithm of the neutron reflectivity plotted as a function of the neutron momentum transfer, Q . Panels (C), (F), and (I) show the spatial distributions of the different components derived from the model fits to the neutron reflectivity data. The fully deuterated dRcLPS/dDPPC bilayer data (A,D,G) highlighted the amount and location of h-AMP as bound across the interface; partially deuterated hRcLPS/dDPPC bilayer data (B,E,H) illustrated the lipid bilayer structure after AMP binding. In panels (C), (F), and (I), the first layer from 0 to 14 \AA refers to the SiO_2 layer but the volume fractions of SiO_2 are not presented.

of z (distance along the surface normal direction) (Table S5). NR revealed that the LPS monolayers had thicknesses of 13 ± 1 and 23 ± 2 \AA (Figure 4B) for the tail layer and head layer, respectively. The surface coverage as calculated from the surface concentration was 0.84 ± 8 $\mu\text{mol}/\text{m}^2$, and the area per molecule was 198 ± 20 \AA^2 . G_3 and C_8G_2 were then injected in the bulk solution under the LPS monolayer to a final concentration of 30 μM . Rapid surface pressure increases were observed caused by AMP binding and α -helical transformation (Figures S5 and S6). Fitting of NR data (Figure 4C,E) revealed the adsorption of AMPs into the LPS head group regions, with some insertion of the peptides into the hydrophobic acyl chain regions (Figure 4D,F). There is also evidence of the formation of LPS/AMP aggregates associated with the lipid monolayer, shown as stack layers. Across the LPS monolayer, G_3 had evenly distributed surface concentrations of 0.34, 0.33, and 0.26 $\mu\text{mol}/\text{m}^2$ in the tail, head, and underlying stack layers, respectively. Some 34% of LPS molecules were found to be displaced by G_3 from the primary spread monolayer, while 12% of LPS molecules were aggregated with G_3 and suspended outside the lipid head groups, with a thickness of 36 ± 3 \AA . In contrast, C_8G_2 had surface concentrations distributed among the same three layers of 0.64, 0.12, and 0.18 $\mu\text{mol}/\text{m}^2$, respectively, indicating quick penetration into the LPS tail region (68% of total AMP molecules). Lipid removal was more significant (51%), and the stack layer was thinner (25 ± 2 \AA) than for G_3 , and the proportion of lipids resuspended outside the lipid head layer was only 4%. The NR study from the spread LPS monolayers revealed lipid membrane fusion and disruption caused by both G_3 and C_8G_2 , although not as significantly as in the vesicles

measured by SANS. However, G_3 evidently caused more overall structural disruption, as evidenced by the formation of expanded membrane stacks under the LPS monolayer. In contrast, C_8G_2 removed more lipids from the primary spread monolayer and was more extensively inserted into the remaining monolayer, but its underlying membrane stacks were thinner and contained less C_8G_2 and lipids.

3.5. Supported Lipid Bilayer Model. The spread lipid monolayer offers simplicity and enables the most direct structural information to be determined from NR regarding the amount of lipids in the model membrane leaflet, its thickness, and changes in these parameters upon AMP binding. The monolayer study revealed structural differences induced by the two AMPs when disrupting the LPS membrane leaflet. However, the outer acyl chain surface of the spread monolayer is directly exposed to air. For more direct mimicry of the *E. coli* OM and to investigate how each AMP disrupts the LPS membrane more precisely, asymmetric bilayers (LPS/DPPC) were constructed on the SiO_2 substrate. In parallel, supported symmetric POPG/POPC bilayers were used as the IM model (control) to compare their susceptibility to the two AMPs. To enhance the interfacial resolution of the NR measurements, we produced fully deuterated bilayers of dLPS/dDPPC (Figure 5A) and partially deuterated bilayers of hLPS/dDPPC (Figure 5B). Upon interaction with hydrogenated AMP molecules, the AMP location was highlighted using the fully deuterated dLPS/dDPPC bilayers while the structural disorder within the lipid bilayer was identified from the partially deuterated hLPS/dDPPC bilayer. NR measurements using both the deuterated and partially deuterated lipid bilayers were performed under three isotopic solution contrasts (D_2O , CMSi, H_2O) not only

to improve structural resolution, as discussed, but also to characterize the hydration in the different interfacial regions. Unlike the symmetrical three-layer model applied to the bilayer surrounding the SUVs, the four-layer model applied here must be unsymmetrical to take into account the different sizes of the small inner PC head layer and the large outer LPS head layer. The parameters derived from the best model fits are listed in Tables S6–S8, and the fits are plotted as the continuous lines in Figure 5A,B, with the best fit SLD profiles shown in the Figure S7. Figure 5C shows the volume fraction distributions of the different LPS/PL components and indicates high surface packing density of the bilayers at 37 °C. These features are highly consistent with similar bilayer models as previously reported.¹⁸ The DPPC inner leaflet and LPS outer leaflet had areas per molecule of 58 ± 6 and 162 ± 16 Å², respectively, equivalent to surface concentrations of 3.05 ± 0.30 and 1.02 ± 0.10 μmol/m², respectively.

Exposure to either G₃ or C₈G₂ substantially increased the thickness of the LPS/DPPC bilayers, as is evident from the shifts of the interference fringes⁵² in the reflectivity profiles measured in D₂O (black curves in Figure 5B,E,H). Binding of G₃ to the LPS/DPPC bilayers led to lipid fusion, which is characterized by the occurrence of the Bragg peaks as evident in Figure 5D,E at $Q = 0.11$ Å⁻¹. These features can be identified as two bilayers (thickness = 153 Å) after simultaneous fitting of the six isotopic contrasts (Figure 5F). The best fit analysis revealed that $17 \pm 2\%$ of DPPC and $37 \pm 3\%$ of LPS molecules were removed from the bilayer upon G₃ binding and insertion, with noticeable increases in the overall thickness of the bilayer. Furthermore, $13 \pm 1\%$ DPPC and $10 \pm 1\%$ LPS molecules became suspended outside the original bilayer, bridged by a 23 Å gap layer rich in G₃ aggregates and LPS core segments.

By contrast, C₈G₂ became directly inserted into the LPS/DPPC bilayer and its volume fraction distribution across the LPS/DPPC bilayer was significantly higher than for G₃ (Figure 5I). Although the overall amounts of G₃ and C₈G₂ bound into the bilayers are broadly similar (1.43 and 1.63 μmol/m², respectively), C₈G₂ has a higher volume fraction (~30%) in the acyl chain region of the DPPC inner leaflet. DPPC was not largely disrupted by the AMP, but 61% of the LPS molecules were removed from the surface and 38% of them were co-aggregated with C₈G₂ molecules outside the LPS head group layer as depicted in Figure 5I. The LPS removal and the adsorbed AMPs within the LPS layers were broadly similar for the LPS/DPPC bilayer and LPS monolayer models.

Similar analysis was also undertaken for the supported symmetric POPG/POPC (3:7, mol/mol) bilayers, with a best fit head layer thickness of 8 ± 1 Å and middle acyl chain layer thickness of 32 ± 3 Å (Figure S8). Upon exposure to the AMPs, the symmetrical bilayers remained but with a small amount of AMP bound and inserted. At an AMP concentration of 10 μM, 0.40 ± 0.04 μmol/m² of G₃ and 0.67 ± 0.06 μmol/m² of C₈G₂ were embedded in the IM bilayers, meaning that there were 21 and 32% lipid removal, respectively. Detailed NR parameters of the POPG/POPC bilayers are listed in Tables S9–S11. Unlike the results from the bacterial OM model, where there was very significant peptide interaction and the formation of lipid stacks, the IM bilayers experienced significantly lower AMP binding and lipid removal. NR measurements of the supported bilayers suggested that both G₃ and C₈G₂ can disrupt bacterial IM and OM bilayers and hence kill bacteria. G₃ is efficient in

reorganizing the LPS-dominated OM, while C₈G₂ is less selective and disrupting either the OM or IM.

4. DISCUSSION

The number of positive charges and hydrophobicity are the two main parameters used to manipulate AMP design, and their interplay is often supported by transitions to amphiphilic secondary structures and adjustment to the self-assembly process.^{3,4} These factors directly affect the membrane disruption efficiency and bactericidal activity of amphiphilic AMPs. Most currently reported AMPs are designed to disrupt bacterial cytoplasmic membranes rather than the bacterial outer membranes. This is mainly due to the wide recognition of the crucial relevance of the IM in bactericidal action. However, it has become clear that the exact structure and composition of bacterial membranes are important. This is because there are large variations in cell membranes between different bacteria, and it is crucial to understand how AMPs interact with key membrane components using specific model studies. For Gram-negative bacteria, both the OM and IM affect the performance of an AMP, but the OM tends to be more difficult to study due to the lack of credible samples, such as well-purified deuterated LPS.

Given the large differences in the structure and composition between the bacterial outer leaflet of the OM (lipopolysaccharide or peptidoglycan) and that of the bacterial IM (phospholipids), AMP design must consider how to target these different membrane components possessing different structures and physiochemical properties. The strongly cationic G₃ was designed to specifically target the LPS of *E. coli*, while the hydrophobic C₈G₂ has strong potency against both the IM and OM with relatively low selectivity. Since the bacterial OM serves as the first barrier against antibiotics and is therefore implicated in antimicrobial resistance,⁸ the design of OM-specific AMPs may provide a better route for the development of potent AMPs to treat infections from antimicrobial-resistant strains, such as ESBL *E. coli*.

The two cationic AMPs studied here adopted random-coil conformations in buffer (Figure 3A,B) and showed a weak propensity to self-assemble when exposed to the uncharged membranes that mimic those of host cells. G₃ and C₈G₂ both had low cytotoxicity to hRBCs with an EC₅₀ ranging from 550 to 650 μM. However, the peptides transformed into α -helical conformations and tended to form nanoaggregates once bound to anionic bacterial membrane mimics but then displayed potent membrane-disruptive activity. AMP-rich nanostructures are formed and often described by barrel-stave pore, toroidal pore, and carpet models.⁸ Antimicrobial experiments indicated that both G₃ and C₈G₂ were potent against *E. coli*, with MICs around 10 μM. Importantly, these designed AMPs showed rapid bactericidal activity against *E. coli* within 5–10 min of interaction. By comparison, traditional antibiotics require hours of exposure to kill bacteria under similar conditions, consistent with other studies.^{7,12,38} Due to this rapid membrane disruptive mechanism, AMPs are less likely to develop antimicrobial susceptibility or resistance.

Various lipid models, developed from the main IM and OM components of *E. coli*, facilitated the use of different techniques to investigate the structures and interactions underlying the antimicrobial potency and selectivity. Vesicular models composed of POPG/POPC or LPS/POPC were used to mimic the *E. coli* IM and OM. SANS measurements (Figure 3C) showed that G₃ caused substantial lipid bilayer fusion in

the LPS/POPC SUVs, with the formation of bilayer stacks each with a repeat thickness around 60 Å. By contrast, lipid fusion by C_8G_2 was not as evident as for G_3 (Figure 3D). This difference suggests a different mode of attack by C_8G_2 due to its smaller number of charges and greater hydrophobicity. However, neither G_3 nor C_8G_2 was found to cause any drastic structural change to the bacterial IM vesicles, even though both displayed similar insertion into the model membrane bilayer (Figure S3A). As the negatively charged LPS and POPG had the same mass ratio of about 30%, their strength of interaction with AMPs could be directly compared. The stronger G_3 -LPS fusion, driven by the electrostatic interaction, dominates the disruption of the bacterial OM. ^{31}P and 2H ss-NMR measurements demonstrated the dynamic processes associated with the lipid phosphate head groups and acyl chain deuterated tail groups, indicating a loss of local order and gain in the fluidity of the lipid hydrocarbon chains associated with the insertion of the AMPs, especially G_3 . However, neither G_3 nor C_8G_2 was found to impose any significant influence on the order of the lipid heads despite the formation of lipid stacks induced by their co-assembly with G_3 molecules. However, both SANS and ss-NMR revealed greater potency of the cationic G_3 against the *E. coli* OM model, which would translate into stronger antibacterial activity against *E. coli*.

To further determine the extent of membrane damage, we also constructed planar LPS monolayer, asymmetric LPS/DPPC bilayer, and symmetric POPG/POPC bilayer models and used NR to investigate the AMP-LPS interactions with a spatial resolution of 1–2 Å. Through the combined use of deuterium labeling of lipids and buffer solution, the amounts and locations of different components of the bilayer-AMP constructs (inner DPPC leaflet, outer LPS leaflet, AMP, hydration, and relative locations) could be calculated. The results are shown in the form of volume fraction distributions (Figures 4B,D,F and 5C,F,I). G_3 is highly selective against the OM, showing more binding and structural damage against this than against the IM. G_3 binding removed some LPS molecules from the original monolayer or bilayer, with some of the removed LPS molecules reassembling into bilayer stacks on the outer surface of the original membrane. These lipid stacks were evident in both the supported bilayer and vesicle models but less obvious from the spread monolayer model. This is because the primary LPS monolayer is thinner and does not contribute to the interference fringe formed by the small bilayer stacks. However, the NR analysis from the spread LPS monolayer did reveal the formation of large G_3 -LPS stacks/aggregates underneath the original spread monolayer, forming an additional layer some 36 ± 3 Å thick, which is broadly consistent with the measurements of lipid stacks underneath the supported bilayer. Due to its structural simplicity, the monolayer model offers higher resolution when measured under the different isotopic contrasts. In addition to the formation of the underlying G_3 -lipid bilayer stacks, information about the amount of LPS removal and the extent of AMP insertion was also determined.

In comparison, the same data analysis approach revealed that C_8G_2 became directly inserted into both the IM and OM models. While less effective in promoting lipid stacks, it is more effective at removing lipids. There is a high amount of C_8G_2 binding and penetration, consistent with its greater hydrophobicity. Like C_8G_2 , many AMPs are designed to have strong penetration capability and form membrane-bound or inserted AMP nanoaggregates. However, if the peptide is too

hydrophobic there may be a tendency for many of the AMP molecules to aggregate in the bulk and/or adsorb on bacterial membranes, leading to reduced antimicrobial activity and efficiency. Such peptides may also lose specificity against polyanionic bacteria. However, these hydrophobic molecules can be efficient in killing bacteria on oil-like and less anionic surfaces, which is the case with some antibiotic-resistant strains.

Some hydrophobic AMPs can self-assemble to form hydrogels.⁵³ Furthermore, many applications could use self-assembled nanoaggregates as a reservoir for controlled drug delivery.⁵⁴ To this extent, G_3 is highly potent against the OM of Gram-negative *E. coli*, with well-balanced amphiphilicity and high solubility in physiologically mimicking solutions, but these G_3 features carry with them slightly higher toxicity. The different mode of action by C_8G_2 makes it slightly less potent against *E. coli* but more effective against other bacteria like *S. aureus*,^{32,40} while its self-assembling properties make it ideally suitable for applications where controlled release is desired, e.g., in infection prevention and wound treatment.

5. CONCLUSIONS

This work demonstrates that the interplay between positive charges and hydrophobicity can be exploited in AMP design to render different modes of membrane disruption and cytotoxicity. Strongly cationic G_3 co-assembles with bacterial OMs to form AMP-lipid stacks, thus destroying membrane integrity and creating channels for AMP intake, causing further membrane damage. However, strong cationicity limits the disruption of polyanionic membranes, with greater cytotoxicity at low concentrations. The more hydrophobic C_8G_2 showed slightly worse potency toward *E. coli*, but may have stronger antimicrobial activity against less anionic bacteria, and had better biocompatibility over a wider concentration range. This characteristic, together with its greater propensity to self-assemble, makes C_8G_2 attractive for infection control and wound treatment where prolonged release is desired. By taking advantage of charge and amphiphilic properties, AMPs could be designed to be strain-specific and tuned for specific application. This work has provided useful guidance for the development of more potent and highly selective AMPs to treat Gram-negative bacteria infections.

■ ASSOCIATED CONTENT

Supporting Information

The Supporting Information is available free of charge at <https://pubs.acs.org/doi/10.1021/acsami.1c01643>.

Additional characterization data for the AMP/LPS systems and details of the SANS, ssNMR, surface pressure, FTIR, and NR measurements (PDF)

■ AUTHOR INFORMATION

Corresponding Author

Jian Ren Lu – Biological Physics Laboratory, Department of Physics and Astronomy, Faculty of Science and Engineering, The University of Manchester, Manchester M13 9PL, UK; orcid.org/0000-0001-5648-3564; Phone: 0044 161 200 3926; Email: j.lu@manchester.ac.uk

Authors

Haoning Gong – Biological Physics Laboratory, Department of Physics and Astronomy, Faculty of Science and

Engineering, The University of Manchester, Manchester M13 9PL, UK; Division of Pharmacy and Optometry, Faculty of Biology, Medicine and Health, The University of Manchester, Manchester M13 9PL, UK

Xuzhi Hu – Biological Physics Laboratory, Department of Physics and Astronomy, Faculty of Science and Engineering, The University of Manchester, Manchester M13 9PL, UK; orcid.org/0000-0002-9246-7040

Mingrui Liao – Biological Physics Laboratory, Department of Physics and Astronomy, Faculty of Science and Engineering, The University of Manchester, Manchester M13 9PL, UK; Division of Pharmacy and Optometry, Faculty of Biology, Medicine and Health, The University of Manchester, Manchester M13 9PL, UK

Ke Fa – Biological Physics Laboratory, Department of Physics and Astronomy, Faculty of Science and Engineering, The University of Manchester, Manchester M13 9PL, UK

Daniela Ciurac – Biological Physics Laboratory, Department of Physics and Astronomy, Faculty of Science and Engineering, The University of Manchester, Manchester M13 9PL, UK

Luke A. Clifton – ISIS Pulsed Neutron & Muon Source, STFC Rutherford Appleton Laboratory, Harwell Campus, Didcot OX11 0QX, UK; orcid.org/0000-0001-8754-362X

Marc-Antoine Sani – School of Chemistry, Bio21 Institute, University of Melbourne, Melbourne, VIC 3010, Australia; orcid.org/0000-0003-3284-2176

Stephen M. King – ISIS Pulsed Neutron & Muon Source, STFC Rutherford Appleton Laboratory, Harwell Campus, Didcot OX11 0QX, UK; orcid.org/0000-0003-3386-9151

Armando Maestro – Institute Laue Langevin, 38042 Grenoble, France; orcid.org/0000-0002-7791-8130

Frances Separovic – School of Chemistry, Bio21 Institute, University of Melbourne, Melbourne, VIC 3010, Australia; orcid.org/0000-0002-6484-2763

Thomas A. Waigh – Biological Physics Laboratory, Department of Physics and Astronomy, Faculty of Science and Engineering, The University of Manchester, Manchester M13 9PL, UK; orcid.org/0000-0002-7084-559X

Hai Xu – State Key Laboratory of Heavy Oil Processing and the Centre for Bioengineering and Biotechnology, China University of Petroleum (East China), Qingdao 266580, China; orcid.org/0000-0002-5796-4404

Andrew J. McBain – Division of Pharmacy and Optometry, Faculty of Biology, Medicine and Health, The University of Manchester, Manchester M13 9PL, UK

Complete contact information is available at:
<https://pubs.acs.org/10.1021/acsami.1c01643>

Author Contributions

H.G. performed the experiments, data analysis, and manuscript drafting. X.H., M.L., and K.F. undertook LPS extraction and purification and SANS/NR analysis. L.A.C. and H.G. produced the lipid bilayers and supported the NR experiments. M.-A.S. and F.S. supported the ss-NMR experiments and data analysis. S.M.K. and A.M. supported the SANS and NR experiments and data analysis. T.A.W., H.X., and A.J.M. contributed to the research planning and paper writing. J.R.L. conducted research design, planning, funding, paper writing, and finalizing.

Notes

The authors declare no competing financial interest.

ACKNOWLEDGMENTS

We are grateful to the University of Manchester, the China Scholarship Council, Syngenta, Lonza, and STFC for sponsoring H.G., X.H., M.L., and K.F. The authors would also like to thank Dr. Reynard Spiess, Dr. Rehana Sung, and Dr. Derren Heyes for their assistance with MS, HPLC, and CD experiments. We gratefully acknowledge the neutron beam time awarded by the ISIS Pulsed Neutron Source ([10.5286/ISIS.E.RB1920157](https://doi.org/10.5286/ISIS.E.RB1920157), [10.5286/ISIS.E.RB1910068](https://doi.org/10.5286/ISIS.E.RB1910068), [10.5286/ISIS.E.RB1910071](https://doi.org/10.5286/ISIS.E.RB1910071), [10.5286/ISIS.E.RB1720227](https://doi.org/10.5286/ISIS.E.RB1720227)) and the ILL neutron facility ([10.5291/ILL-DATA.TEST-2894](https://doi.org/10.5291/ILL-DATA.TEST-2894)). This work benefited from the use of the SasView application, originally developed under NSF award DMR-0520547. SasView contains code developed with funding from the European Union's Horizon 2020 research and innovation programme under the SINE2020 project, grant agreement No 654000. We thank a European grant from a Marie Curie Fellowship ITN (grant number 608184) under SNAL (small nano-objects for alteration of lipid bilayers), a BBSRC LINK grant with AstraZeneca (BB/S018492/1), and an Innovate UK Knowledge Transfer Partnership project with Lonza under KTP 10809.

REFERENCES

- (1) Carlet, J.; Collignon, P.; Goldmann, D.; Goossens, H.; Gyssens, I. C.; Harbarth, S.; Jarlier, V.; Levy, S. B.; N'Doye, B.; Pittet, D.; Richtmann, R.; Seto, W. H.; van der Meer, J. W. M.; Voss, A. Society's Failure to Protect a Precious Resource: Antibiotics. *Lancet* **2011**, 378, 369–371.
- (2) Laxminarayan, R.; Duse, A.; Wattal, C.; Zaidi, A. K. M.; Wertheim, H. F. L.; Sumpradit, N.; Vlieghe, E.; Hara, G. L.; Gould, I. M.; Goossens, H.; Greko, C.; So, A. D.; Bigdeli, M.; Tomson, G.; Woodhouse, W.; Ombaka, E.; Peralta, A. Q.; Qamar, F. N.; Mir, F.; Kariuki, S.; Bhutta, Z. A.; Coates, A.; Bergstrom, R.; Wright, G. D.; Brown, E. D.; Cars, O. Antibiotic Resistance—the Need for Global Solutions. *Lancet Infect. Dis.* **2013**, 13, 1057–1098.
- (3) Zasloff, M. Antimicrobial Peptides of Multicellular Organisms. *Nature* **2002**, 415, 389–395.
- (4) Mookherjee, N.; Anderson, M. A.; Haagsman, H. P.; Davidson, D. J. Antimicrobial Host Defence Peptides: Functions and Clinical Potential. *Nat. Rev. Drug Discovery* **2020**, 19, 311–332.
- (5) Yeaman, M. R.; Yount, N. Y. Mechanisms of Antimicrobial Peptide Action and Resistance. *Pharmacol. Rev.* **2003**, 55, 27–55.
- (6) Tenover, F. C. Mechanisms of Antimicrobial Resistance in Bacteria. *Am. J. Med.* **2006**, 119, S3–S10.
- (7) Lazzaro, B. P.; Zasloff, M.; Rolff, J. Antimicrobial Peptides: Application Informed by Evolution. *Science* **2020**, 368, eaau5480.
- (8) Ciurac, D.; Gong, H.; Hu, X.; Lu, J. R. Membrane Targeting Cationic Antimicrobial Peptides. *J. Colloid Interface Sci.* **2019**, 537, 163–185.
- (9) Lázár, V.; Martins, A.; Spohn, R.; Daruka, L.; Grézal, G.; Fekete, G.; Számel, M.; Jangir, P. K.; Kintses, B.; Csörgő, B.; Nyerges, Á.; Györkei, A.; Kincses, A.; Dér, A.; Walter, F. R.; Deli, M. A.; Urbán, E.; Hegedűs, Z.; Olajos, G.; Méhi, O.; Bálint, B.; Nagy, I.; Martinek, T. A.; Papp, B.; Pál, C. Antibiotic-Resistant Bacteria Show Widespread Collateral Sensitivity to Antimicrobial Peptides. *Nat. Microbiol.* **2018**, 3, 718–731.
- (10) Ciurac, D.; Campbell, R. A.; Xu, H.; Clifton, L. A.; Hughes, A. V.; Webster, J. R. P.; Lu, J. R. Implications of Lipid Monolayer Charge Characteristics on Their Selective Interactions with a Short Antimicrobial Peptide. *Colloids Surf., B* **2017**, 150, 308–316.
- (11) Ciurac, D.; Campbell, R. A.; Clifton, L. A.; Xu, H.; Fragneto, G.; Lu, J. R. Influence of Acyl Chain Saturation on the Membrane-

Binding Activity of a Short Antimicrobial Peptide. *ACS Omega* **2017**, *2*, 7482–7492.

(12) Gong, H.; Liao, M.; Hu, X.; Fa, K.; Phanphak, S.; Ciunac, D.; Hollowell, P.; Shen, K.; Clifton, L. A.; Campana, M.; Webster, J. R. P.; Fragneto, G.; Waigh, T. A.; McBain, A. J.; Lu, J. R. Aggregated Amphiphilic Antimicrobial Peptides Embedded in Bacterial Membranes. *ACS Appl. Mater. Interfaces* **2020**, *12*, 44420–44432.

(13) Chen, C.; Starr, C. G.; Troendle, E. P.; Wiedman, G.; Wimley, W. C.; Ulmschneider, J. P.; Ulmschneider, M. B. Simulation-Guided Rational de novo Design of a Small Pore-Forming Antimicrobial Peptide. *J. Am. Chem. Soc.* **2019**, *141*, 4839–4848.

(14) Mani, R.; Cady, S. D.; Tang, M.; Waring, A. J.; Lehrer, R. I.; Hong, M. Membrane-Dependent Oligomeric Structure and Pore Formation of a β -Hairpin Antimicrobial Peptide in Lipid Bilayers from Solid-State NMR. *Proc. Natl. Acad. Sci. U. S. A.* **2006**, *103*, 16242–16247.

(15) Yang, L.; Harroun, T. A.; Weiss, T. M.; Ding, L.; Huang, H. W. Barrel-Stave Model or Toroidal Model? A Case Study on Melittin Pores. *Biophys. J.* **2001**, *81*, 1475–1485.

(16) Ludtke, S. J.; He, K.; Heller, W. T.; Harroun, T. A.; Yang, L.; Huang, H. W. Membrane Pores Induced by Magainin. *Biochemistry* **1996**, *35*, 13723–13728.

(17) Fernandez, D. I.; Le Brun, A. P.; Whitwell, T. C.; Sani, M.-A.; James, M.; Separovic, F. The Antimicrobial Peptide Aurein 1.2 Disrupts Model Membranes via the Carpet Mechanism. *Phys. Chem. Chem. Phys.* **2012**, *14*, 15739–15751.

(18) Paracini, N.; Clifton, L. A.; Skoda, M. W. A.; Lakey, J. H. Liquid Crystalline Bacterial Outer Membranes are Critical for Antibiotic Susceptibility. *Proc. Natl. Acad. Sci. U. S. A.* **2018**, *115*, E7587–E7594.

(19) Ma, B.; Fang, C.; Lu, L.; Wang, M.; Xue, X.; Zhou, Y.; Li, M.; Hu, Y.; Luo, X.; Hou, Z. The Antimicrobial Peptide Thanatin Disrupts the Bacterial Outer Membrane and Inactivates the NDM-1 Metallo- β -Lactamase. *Nat. Commun.* **2019**, *10*, 3517.

(20) Dong, H.; Xiang, Q.; Gu, Y.; Wang, Z.; Paterson, N. G.; Stansfeld, P. J.; He, C.; Zhang, Y.; Wang, W.; Dong, C. Structural Basis for Outer Membrane Lipopolysaccharide Insertion. *Nature* **2014**, *511*, 52–56.

(21) Okuda, S.; Sherman, D. J.; Silhavy, T. J.; Ruiz, N.; Kahne, D. Lipopolysaccharide Transport and Assembly at the Outer Membrane: the PEZ Model. *Nat. Rev. Microbiol.* **2016**, *14*, 337–345.

(22) Raetz, C. R. H.; Whitfield, C. Lipopolysaccharide Endotoxins. *Annu. Rev. Biochem.* **2002**, *71*, 635–700.

(23) Clifton, L. A.; Skoda, M. W. A.; Le Brun, A. P.; Ciesielski, F.; Kuzmenko, I.; Holt, S. A.; Lakey, J. H. Effect of Divalent Cation Removal on the Structure of Gram-Negative Bacterial Outer Membrane Models. *Langmuir* **2015**, *31*, 404–412.

(24) Zhang, G.; Meredith, T. C.; Kahne, D. On the Essentiality of Lipopolysaccharide to Gram-Negative Bacteria. *Curr. Opin. Microbiol.* **2013**, *16*, 779–785.

(25) Wiener, M. C.; Horanyi, P. S. How Hydrophobic Molecules Traverse the Outer Membranes of Gram-Negative Bacteria. *Proc. Natl. Acad. Sci. U. S. A.* **2011**, *108*, 10929–10930.

(26) Mukherjee, S.; Zheng, H.; Derebe, M. G.; Callenberg, K. M.; Partch, C. L.; Rollins, D.; Propheter, D. C.; Rizo, J.; Grabe, M.; Jiang, Q.-X.; Hooper, L. V. Antibacterial Membrane Attack by a Pore-Forming Intestinal C-Type Lectin. *Nature* **2014**, *505*, 103–107.

(27) Morrison, D. C.; Jacobs, D. M. Binding of Polymyxin B to the Lipid A Portion of Bacterial Lipopolysaccharides. *Immunochemistry* **1976**, *13*, 813–818.

(28) Hu, J.; Chen, C.; Zhang, S.; Zhao, X.; Xu, H.; Zhao, X.; Lu, J. R. Designed Antimicrobial and Antitumor Peptides with High Selectivity. *Biomacromolecules* **2011**, *12*, 3839–3843.

(29) Chen, C.; Hu, J.; Zeng, P.; Pan, F.; Yaseen, M.; Xu, H.; Lu, J. R. Molecular Mechanisms of Anticancer Action and Cell Selectivity of Short α -Helical Peptides. *Biomaterials* **2014**, *35*, 1552–1561.

(30) Chen, C.; Hu, J.; Zeng, P.; Chen, Y.; Xu, H.; Lu, J. R. High Cell Selectivity and Low-Level Antibacterial Resistance of Designed Amphiphilic Peptide G(IKK)₃-NH₂. *ACS Appl. Mater. Interfaces* **2014**, *6*, 16529–16536.

(31) Liu, K.; Yang, L.; Peng, X.; Wang, J.; Lu, J. R.; Xu, H. Modulation of Antimicrobial Peptide Conformation and Aggregation by Terminal Lipidation and Surfactants. *Langmuir* **2020**, *36*, 1737–1744.

(32) Gong, H.; Sani, M.-A.; Hu, X.; Fa, K.; Hart, J. W.; Liao, M.; Hollowell, P.; Carter, J.; Clifton, L. A.; Campana, M.; Li, P.; King, S. M.; Webster, J. R. P.; Maestro, A.; Zhu, S.; Separovic, F.; Waigh, T. A.; Xu, H.; McBain, A. J.; Lu, J. R. How do Self-Assembling Antimicrobial Lipopeptides Kill Bacteria? *ACS Appl. Mater. Interfaces* **2020**, *12*, 55675–55687.

(33) Le Brun, A. P.; Clifton, L. A.; Halbert, C. E.; Lin, B.; Meron, M.; Holden, P. J.; Lakey, J. H.; Holt, S. A. Structural Characterization of a Model Gram-Negative Bacterial Surface Using Lipopolysaccharides from Rough Strains of Escherichia Coli. *Biomacromolecules* **2013**, *14*, 2014–2022.

(34) Clifton, L. A.; Skoda, M. W. A.; Daulton, E. L.; Hughes, A. V.; Le Brun, A. P.; Lakey, J. H.; Holt, S. A. Asymmetric Phospholipid: Lipopolysaccharide Bilayers; a Gram-Negative Bacterial Outer Membrane Mimic. *J. R. Soc., Interface* **2013**, *10*, 20130810.

(35) Nikaido, H. Molecular Basis of Bacterial Outer Membrane Permeability Revisited. *Microbiol. Mol. Biol. Rev.* **2003**, *67*, 593–656.

(36) Galanos, C.; Lüderitz, O.; Westphal, O. A New Method for the Extraction of R Lipopolysaccharides. *Eur. J. Biochem.* **1969**, *9*, 245–249.

(37) Wiegand, I.; Hilpert, K.; Hancock, R. E. W. Agar and Broth Dilution Methods to Determine the Minimal Inhibitory Concentration (MIC) of Antimicrobial Substances. *Nat. Protoc.* **2008**, *3*, 163–175.

(38) Fantner, G. E.; Barbero, R. J.; Gray, D. S.; Belcher, A. M. Kinetics of Antimicrobial Peptide Activity Measured on Individual Bacterial Cells using High-Speed Atomic Force Microscopy. *Nat. Nanotechnol.* **2010**, *5*, 280–285.

(39) Matsuzaki, K.; Sugishita, K.-I.; Miyajima, K. Interactions of an Antimicrobial Peptide, Magainin 2, with Lipopolysaccharide-Containing Liposomes as a Model for Outer Membranes of Gram-Negative Bacteria. *FEBS Lett.* **1999**, *449*, 221–224.

(40) Gong, H.; Zhang, J.; Hu, X.; Li, Z.; Fa, K.; Liu, H.; Waigh, T. A.; McBain, A.; Lu, J. R. Hydrophobic Control of the Bioactivity and Cytotoxicity of de Novo-Designed Antimicrobial Peptides. *ACS Appl. Mater. Interfaces* **2019**, *11*, 34609–34620.

(41) Pan, F.; Li, Z.; Gong, H.; Petkov, J. T.; Lu, J. R. Membrane-Lytic Actions of Sulphonated Methyl Ester Surfactants and Implications to Bactericidal Effect and Cytotoxicity. *J. Colloid Interface Sci.* **2018**, *531*, 18–27.

(42) Hu, X.; Gong, H.; Li, Z.; Ruane, S.; Liu, H.; Pambou, E.; Bawn, C.; King, S.; Ma, K.; Li, P.; Padia, F.; Bell, G.; Lu, J. R. What Happens When Pesticides are Solubilized in Nonionic Surfactant Micelles. *J. Colloid Interface Sci.* **2019**, *541*, 175–182.

(43) Hu, X.; Gong, H.; Li, Z.; Ruane, S.; Liu, H.; Hollowell, P.; Pambou, E.; Bawn, C.; King, S.; Rogers, S.; Ma, K.; Li, P.; Padia, F.; Bell, G.; Ren, J. How does Solubilisation of Plant Waxes into Nonionic Surfactant Micelles Affect Pesticide Release? *J. Colloid Interface Sci.* **2019**, *556*, 650–657.

(44) Sani, M.-A.; Le Brun, A. P.; Separovic, F. The Antimicrobial Peptide Maculatin Self Assembles in Parallel to Form a Pore in Phospholipid Bilayers. *Biochim. Biophys. Acta, Biomembr.* **2020**, *1862*, 183204.

(45) Webster, J.; Holt, S.; Dalgliesh, R. INTER the Chemical Interfaces Reflectometer on Target Station 2 at ISIS. *Phys. B* **2006**, *385–386*, 1164–1166.

(46) Campbell, R. A.; Wacklin, H. P.; Sutton, I.; Cubitt, R.; Fragneto, G. FIGARO: The New Horizontal Neutron Reflectometer at the ILL. *Eur. Phys. J. Plus* **2011**, *126*, 107.

(47) Nelson, A. Co-Refinement of Multiple-Contrast Neutron/X-Ray Reflectivity Data Using MOTOFIT. *J. Appl. Crystallogr.* **2006**, *39*, 273–276.

(48) Hancock, R. E. W. Cationic Peptides: Effectors in Innate Immunity and Novel Antimicrobials. *Lancet Infect. Dis.* **2001**, *1*, 156–164.

(49) Greenfield, N. J. Using Circular Dichroism Collected as a Function of Temperature to Determine the Thermodynamics of Protein Unfolding and Binding Interactions. *Nat. Protoc.* **2006**, *1*, 2527–2535.

(50) Silva, T.; Claro, B.; Silva, B. F. B.; Vale, N.; Gomes, P.; Gomes, M. S.; Funari, S. S.; Teixeira, J.; Uhríková, D.; Bastos, M. Unravelling a Mechanism of Action for a Cecropin A-Melittin Hybrid Antimicrobial Peptide: The Induced Formation of Multilamellar Lipid Stacks. *Langmuir* **2018**, *34*, 2158–2170.

(51) Sani, M.-A.; Separovic, F. How Membrane-Active Peptides Get into Lipid Membranes. *Acc. Chem. Res.* **2016**, *49*, 1130–1138.

(52) Clifton, L. A.; Ciesielski, F.; Skoda, M. W. A.; Paracini, N.; Holt, S. A.; Lakey, J. H. The Effect of Lipopolysaccharide Core Oligosaccharide Size on the Electrostatic Binding of Antimicrobial Proteins to Models of the Gram Negative Bacterial Outer Membrane. *Langmuir* **2016**, *32*, 3485–3494.

(53) Schnaider, L.; Brahmachari, S.; Schmidt, N. W.; Mensa, B.; Shaham-Niv, S.; Bychenko, D.; Adler-Abramovich, L.; Shimon, L. J. W.; Kolusheva, S.; DeGrado, W. F.; Gazit, E. Self-Assembling Dipeptide Antibacterial Nanostructures with Membrane Disrupting Activity. *Nat. Commun.* **2017**, *8*, 1365.

(54) Cao, M.; Zhao, W.; Wang, L.; Li, R.; Gong, H.; Zhang, Y.; Xu, H.; Lu, J. R. Graphene Oxide-Assisted Accumulation and Layer-by-Layer Assembly of Antibacterial Peptide for Sustained Release Applications. *ACS Appl. Mater. Interfaces* **2018**, *10*, 24937–24946.